Mechanical Systems and Signal Processing 183 (2023) 109584

Contents lists available at ScienceDirect

Mechanical Systems and Signal Processing

journal homepage: www.elsevier.com/locate/ymssp

Enhanced extended state observer-based model-free force control for a Series Elastic Actuator ☆

Shuaishuai Han [a], Haoping Wang [a,*], Yang Tian [a], Haoyong Yu [b]

[a] School of Automation, Nanjing University of Science and Technology, Nanjing 210094, China
[b] Department of Biomedical Engineering, National University of Singapore, Singapore 117583, Singapore

ARTICLE INFO

Communicated by J. RODELLAR

Keywords:
Series Elastic Actuator
Model-free force control
Enhanced extended state observer

ABSTRACT

With inherent mechanical compliance and programmable force controllability, the Series Elastic Actuator (SEA) has been a popular choice for modern mechanical systems. It is crucial to realize accurate and robust force control for a SEA, especially in a physical human–robot interaction condition. In this paper, a model-free force controller (MFFC) for the SEA is developed, which relies only on the input–output measurement. Firstly, based on the *ultra-local model* concept, the SEA force dynamics is reformulated in a simpler way, and all unknown terms are grouped as one term called *lumped total disturbance*. Secondly, an enhanced extended stated observer (EESO) is designed to simultaneously estimate the *lumped total disturbance*, the force velocity, and the control input gain. Thirdly, a disturbance rejective intelligent PD (iPD) control scheme is established. In addition, the effects of the control input gain are analyzed and the close-loop stability is demonstrated with Lyapunov method. The control accuracy and robustness of the MFFC are verified in a physical human–robot interaction environment.

1. Introduction

Series Elastic Actuators (SEAs) have attracted increasing attention since the initial concept was formally introduced in [1]. Various mechanical or mechatronic systems have adopted SEAs, especially the advanced robots like wearable exoskeletons [2], humanoid robots [3] and haptic robots [4]. Compared to conventional high-stiffness actuators, SEAs can perform a better control of human–robot interaction with mechanical compliance, force-sensing capability and programmable force controllability. Meanwhile, satisfactory human–robot interaction or robot–environment interaction requires high performance in force control.

The PID-type controllers with various parameter tuning methods or compensation techniques [1,5] have been preferable in force control of the SEA. In [6], a linear quadratic regulation (LQR) method was used to obtain suitable PD control parameters. To enhance the robustness of force control, the authors in [7] added a feedforward term for a conventional PID controller. However, when mechanical drawbacks (friction, backlash) or external forces (human–robot interaction, unknown load-side dynamics [8]) are evident, a PID-type controller can hardly achieve accurate force tracking.

Disturbance observer (DOB) is a popular and practical choice to improve the robustness and accuracy of force control in the face of various uncertainties and external disturbances. In [3,9], conventional DOBs were used to improve the force control performance of different SEAs. In [10], a second-order DOB was designed to estimate the disturbance force and its first and second-order values.

☆ This work was supported in part by Agency for Science, Technology and Research, Singapore, under the National Robotics Program, with A*star SERC Grant No.: 192 25 00054 and National Natural Science Foundation of China under Grants 62173182, 61773212. S. Han would like to thank the China Scholarship Council (CSC) for supporting his visiting in Singapore.

* Corresponding author.
E-mail addresses: hp.wang@njust.edu.cn (H. Wang), bieyhy@nus.edu.sg (H. Yu).

https://doi.org/10.1016/j.ymssp.2022.109584
Received 20 February 2022; Received in revised form 18 June 2022; Accepted 15 July 2022
Available online 1 August 2022

However, as the inverse dynamics was needed, the dynamics of SEAs had to be identified, and additional filters were required to implement conventional DOBs. Meanwhile, the performance of such DOB-based control is limited by the mismatch from the identified model [11].

Other modern control theories can also be applied to the design of SEA controller, like singular perturbation-based control [12], adaptive control [8], learning control [13,14] and etc. The main drawback of these theories is the requirement of precise modeling or the complexity of implementation. Besides, most of the publications did not consider the interactive forces from the environment or humans, but the performance of force control will generally get degraded under interactive conditions [6].

Model-free control [15,16], which relies only on the input–output measurement, can overcome the limitations of modeling mismatch and guarantee the robustness to external disturbances and internal uncertainties. Based on the concept of *ultra-local model* [15], all the unknown terms are grouped in a single term called *lumped total disturbance*. Then an intelligent PD (iPD) control scheme can be constructed with the estimate of *lumped total disturbance*. Meanwhile, for the implementation of this method to the SEA force control, three issues need to be solved, which are the estimation of *lumped total disturbance*, the estimation of velocity and the determination of control input gain.

The extended state observer (ESO) [17,18] can simultaneously perform disturbance estimation and velocity estimation. Since proposed in [19] with a powerful bandwidth tuning method, the linear ESO (LESO) has gotten widely applied because of the simplicity during implementation. In order to improve the adaptability, adaptive theory have been combined to ESO-based control to develop adaptive ESO [20–22] or ESO-based adaptive feedback control [23,24]. However, model identification may be still needed [22,23], and the complexity of adaptive design will make it time-consuming to apply such controllers. Besides, few of the existing publications gave the solution of selecting the control input gain, which is still an open problem in model-free control [25,26]. In [25], the authors focused on the control of a globally Lipschitz nonlinear discrete-time system which is nonaffine to control inputs. The LESO was adopted with online estimation of control input gain, which is achieved by sampling and delayed signal. In [26], the ESO was formulated obeying high-gain design principle as [27] and a projected gradient estimator (PGE) was designed to estimate the input uncertainties. Nevertheless, the possible peak phenomenon still cannot be avoided. Besides, both of the two papers were interested in the control problem of a general system and a main focus of them is theoretical stability and convergence, instead of practical applications. Only simulation results were provided in [25,26] and the feasibility still needs to be verified during real-world applications.

In this paper, the LESO [19] is modified to an enhanced ESO (EESO), which is capable of estimating the *lumped total disturbance*, the force velocity and the control input gain simultaneously. The effects of the control input gain are analyzed by simulation and experiments, which have been rarely reported. With the *ultra-local model* and the EESO, the proposed MFFC is finally achievable and entirely model-free. In fact, this kind of controller has rarely been reported in the SEA-related publications. The main contributions of this paper can be summarized as follows:

1. A novel EESO-based MFFC (EESO-MFFC) is developed and applied to achieve accurate and robust force control of a low-stiffness SEA. The proposed controller avoids model identification and needs only the input–output measurement. The control parameters can be easily tuned with eigenvalue assignment technique and bandwidth concept. Close-loop stability analysis is provided with Lyapunov approach.
2. Compared to existing popular SEA force controllers and other model-free methods, the proposed controller can achieve better robustness and accuracy with minimal modeling information. The control performance is verified with an SEA-driven robotic arm in several cases including force trajectory tracking, zero force control, and joint-level impedance control. Such a method is not only suitable for linear SEA, but also extendable to nonlinear SEA or variable stiffness actuators.

The rest of this paper is organized as follows. In Section 2, the SEA prototype and the force dynamics are presented. Section 3 introduces the design procedure of the EESO-MFFC scheme. In Section 4, the proposed EESO-MFFC is verified with comparative experiments in a human–robot interaction environment. Finally, Section 5 is dedicated to the conclusion and future work.

2. Dynamic analysis and modeling of the SEA

The CAD prototype and the hardware components of the SEA studied in this paper are illustrated in Fig. 1.

As shown in Fig. 1, the SEA consists mainly of a driven motor (Maxon EC-4pole), a torsion spring, two linear springs, a ball screw, two rotary encoders for motor and ball screw, a linear potentiometer to measure the deformation of the linear spring and a torsional potentiometer to measure the position of the robot joint. The SEA joint is driven by tension cables. As it contains two low-stiffness linear springs and one high-stiffness torsion spring, the SEA can work at two different force levels. Table 1 gives the physical parameters of the SEA. In this paper, we mainly focus on the force control with linear springs. In previous publications [6,11], an equivalent model is usually used to describe the dynamics of SEA. In this work, we directly use all the physical parameters and dynamic structures to analyze the dynamic process. The modeling process of the SEA can be illustrated as Fig. 2.

The dynamics from the motor to the ball screw is

$$J_m\ddot{\theta}_m + b_m\dot{\theta}_m + \tau_t = k_m i_c = \tau_m \tag{1}$$

where θ_m denotes the angle of the motor, τ_m denotes motor torque, J_m denotes inertia of the motor, b_m denotes damping of the motor, k_m denotes torque constant of the motor, and i_c denotes control current. τ_t is the torque exerted on the ball screw from the motor side. Then, from the ball screw to the cable tension, one has

$$J_{screw}\ddot{\theta}_{screw} + f\left(\dot{\theta}_{screw}\right) + \frac{p}{2\pi}F = \tau_t, \tag{2}$$

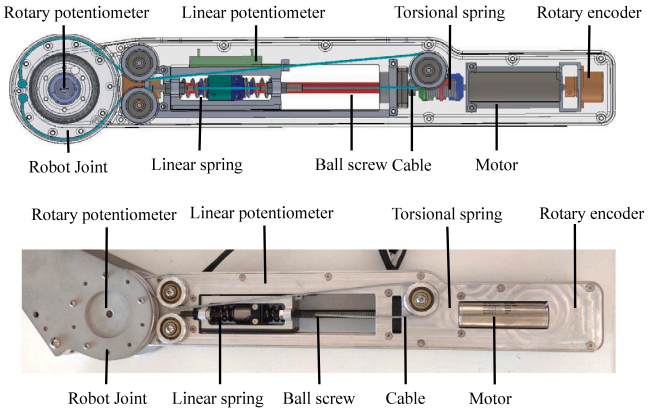

Fig. 1. The CAD prototype (top) and hardware (bottom) of the studied SEA.

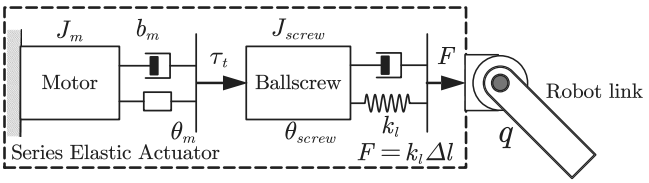

Fig. 2. Modeling illustration of the SEA.

Table 1
Physical parameters of SEA.

Symbol	Quantity	Value
J_m	Inertia of the motor	5.517×10^{-6} kg m^2
k_m	Torque constant of the motor	0.0276 Nm/A
J_{screw}	Inertia of the screw	7.406×10^{-6} kg m^2
p	Pitch of the ball screw	2×10^{-3} m
r	Radius of robot joint	0.05 m
k_l	Stiffness of linear spring	2.4×10^4 N/m

where J_{screw} denotes the inertia of the ball screw, θ_{screw} denotes the angle of the ball screw, $f\left(\dot{\theta}_{screw}\right)$ is the nonlinear friction from the ball screw, p denotes the pitch of the ball screw [6] and F denotes the force generated by the linear springs. In practical applications, the force in the spring measuring range is usually enough for the assistive robots, which is called low force mode in [6]. Therefore, in this work, only the low force range is considered and $\theta_m = \theta_{screw}$. In an ideal case, there is the following relation for the joint angle

$$\Delta l + qr = \frac{p}{2\pi}\theta_m = \frac{p}{2\pi}\theta_{screw}, \tag{3}$$

where q is the angle of the robot joint and r is the radius of the robot joint. Δl is the deformation of the linear spring measured by the linear potentiometer. The output force of the SEA is thus measured as

$$F = k_l \Delta l. \tag{4}$$

By substituting (2),(3),(4) to (1) and cancelling $\theta_m, \tau_t, \Delta l$, the force dynamics of the SEA can be deduced as

$$\begin{aligned}\ddot{F} = &-\frac{b_m}{J_m+J_{screw}}\dot{F} - \left(\frac{p}{2\pi}\right)^2 \frac{k_l}{J_m+J_{screw}} F + \frac{p}{2\pi}\frac{k_l}{J_m+J_{screw}} u \\ &-k_l r\ddot{q} - \frac{k_l}{J_m+J_{screw}} b_m r\dot{q} - \frac{p}{2\pi}\frac{k_l}{J_m+J_{screw}} f\left(\dot{\theta}_{screw}\right)\end{aligned}, \tag{5}$$

where u denotes the control input τ_m. Here an unknown disturbance term can be defined as

$$d = -k_l r\ddot{q} - \frac{k_l b_m r}{J_m + J_{screw}}\dot{q} - \frac{p}{2\pi}\frac{k_l}{J_m + J_{screw}} f\left(\dot{\theta}_{screw}\right). \tag{6}$$

And the parametric parts are also redefined as

$$a_1 = \frac{b_m}{J_m+J_{screw}}, a_2 = \left(\frac{p}{2\pi}\right)^2 \frac{k_l}{J_m+J_{screw}}, b = \frac{p}{2\pi}\frac{k_l}{J_m+J_{screw}}. \tag{7}$$

Then the SEA dynamics is finally formulated as follow

$$\ddot{F} = -a_1\dot{F} - a_2F + bu + d. \tag{8}$$

The disturbance term d includes various negative external and internal factors such as friction, backlash, unknown loads and human-interaction forces.

3. Model-free force control with an enhanced extended state observer

3.1. Ultra-local model-based intelligent PD controller

Although a second-order linear model can be identified, the parameters can only reflect limited dynamics of the SEA. In the proposed control method, only a much simpler *ultra-local model* [15] is needed. Here the *ultra-local model* for the dynamics of the SEA is established as

$$F^{(v)} = d_{lumped} + \alpha u, \tag{9}$$

where α is the control input gain. Generally, α is a non-physical constant parameter chosen by the practitioner so that αu and $F^{(v)}$ have the same magnitude. v is the derivative order and commonly chosen to be 1 or 2. Therefore, the *ultra-local model* can reduce the plant order in some cases. d_{lumped} is called *lumped total disturbance* as it gathers all the effects of unknown dynamics, external disturbance and other uncertainties to a single term.

If $v = 2$ is selected and the unknown d_{lumped} is estimated as $\hat{d}_{lumped}$ and the force derivative is measured, a model-free controller called intelligent PD (iPD) controller can be designed as

$$u = \frac{1}{\alpha}\left(\ddot{F}_d + k_d\dot{e} + k_pe - \hat{d}_{lumped}\right) \tag{10}$$

with

$$e = F_d - F, \dot{e} = \dot{F}_d - \dot{F}, \tag{11}$$

where $F_d, \dot{F}_d, \ddot{F}_d$ are the desired force and its first and second derivatives. By substituting the iPD control law (10) to the *ultra-local model* (9), one can obtain the following error dynamics

$$\ddot{e} + k_d\dot{e} + k_pe = \hat{d}_{lumped} - d_{lumped}. \tag{12}$$

If the lumped total disturbance is effectively estimated and the estimation error is much smaller than the force control error and its derivatives, the error dynamics can be roughly considered as

$$\ddot{e} + k_d\dot{e} + k_pe \approx 0. \tag{13}$$

The control the parameters k_d, k_p can be tuned by eigenvalue assignment technique without much difficulty. For the ease of parametric tuning, following characteristic equation can be proposed

$$\lambda_c(s) = s^2 + k_ds + k_p = (s + \omega_c)^2, \tag{14}$$

where s is the Laplace operator. The eigenvalues are both assigned to be $-\omega_c$. With $k_d = 2\omega_c, k_p = {\omega_c}^2$, the parameters can be easily determined by a single control bandwidth ω_c [19].

3.2. Linear extended state observer-based controller

In order to apply the iPD controller, the LESO can be adopted here to estimate $\dot{F}$ and d_{lumped} at the same time with the only measurable F. To apply the LESO, the SEA dynamics (9) is reformulated in the state space form as

$$\begin{cases} \dot{x}_1 = x_2 \\ \dot{x}_2 = \alpha u + x_3 \\ \dot{x}_3 = \dot{d}_{lumped} \end{cases} \tag{15}$$

with the definition of

$$x_1 = F, x_2 = \dot{F}, x_3 = d_{lumped}, \tag{16}$$

where d_{lumped} is extended to be a new state variable x_3. The corresponding LESO is designed as

$$\begin{cases} \dot{z}_1 = l_1\varepsilon_1 + z_2 \\ \dot{z}_2 = l_2\varepsilon_1 + z_3 + \alpha u \\ \dot{z}_3 = l_3\varepsilon_1 \end{cases} \tag{17}$$

with the observing errors defined as

$$\varepsilon_1 = x_1 - z_1, \varepsilon_2 = x_2 - z_2, \varepsilon_3 = x_3 - z_3, \tag{18}$$

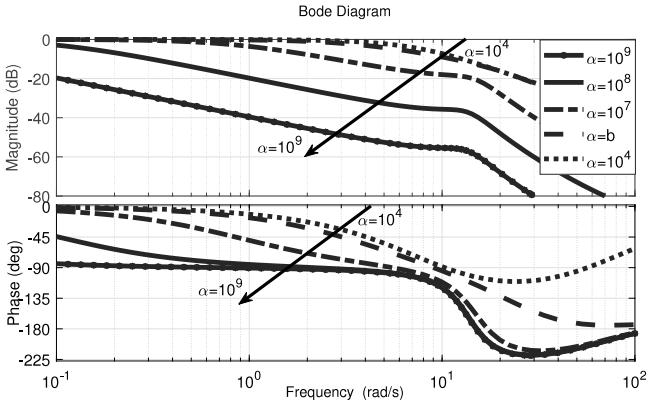

Fig. 3. Close-loop Bode diagram under LESO-MFFC method with different α and $b = 1.45 \times 10^6$ is the actual control input gain in the simulation.

and z_1, z_2, z_3 are the estimates of $F, \dot{F}, d_{lumped}$. l_1, l_2, l_3 are the observer gains to be designed. Therefore, the LESO-based MFFC (LESO-MFFC) is designed as

$$u = \frac{1}{\alpha}\left[\ddot{F}_d + k_d\left(\dot{F}_d - z_2\right) + k_p e - z_3\right]. \tag{19}$$

3.3. Effects of control input gain α

From the error dynamics (12), the selection of control input gain α seems to have no effects on the control stability, as it is cancelled out by the controller design. However, α will have a significant impact on the control performance as it may change the component of d_{lumped}. To date, few researchers have discussed the effects of the control input gain α on model-free control methods. It is generally assumed to be precisely known or obtained by trials. In [28,29], it is proven that the control stability can be guaranteed with a wide range of control input gain. However, from practical tests, the control performance is seriously sensitive to α. In the existing research [15], it is explained that α should make $F^{(v)}$ and αu maintain the same level. Such a state is not explicit and cannot act as a reliable principle. To analyze the effects of α in the closed-loop control system, the authors will deduce the transfer function from F_d (input) to F (output) first.

By substituting the control law (10) to the SEA dynamics (8), one can obtain

$$\ddot{F} + a_1\dot{F} + a_2 F = \frac{b}{\alpha}\left[\ddot{F}_d + k_d\left(\dot{F}_d - \dot{F}\right) + k_p\left(F_d - F\right) - \hat{d}_{lumped}\right] + d \quad . \tag{20}$$

By reformulating (20) in the frequency domain with the Laplace transform, it is possible to obtain

$$\begin{aligned} &F(s)\left[s^2 + \left(a_1 + \frac{b}{\alpha}k_d\right)s + a_2 + \frac{b}{\alpha}k_p\right] \\ &= \frac{b}{\alpha}F_d(s)\left(s^2 + k_d s + k_p\right) - \frac{b}{\alpha}\hat{d}_{lumped}(s) + d(s) \end{aligned} \quad . \tag{21}$$

Since $d(s)$ is unknown, it is ignored and only $\hat{d}_{lumped}(s)$ is considered here. By substituting the control input (10) to the LESO (17), the transfer function from $F_d(s), F(s)$ to $\hat{d}_{lumped}(s)$ is

$$\hat{d}_{lumped}(s) = -\frac{l_3\left(s^2 + k_d s + k_p\right)}{s^3 + l_1 s^2 + l_2 s}\left(F_d(s) - F(s)\right). \tag{22}$$

Then, by substituting (22) to (21), the transfer function from $F_d(s)$ to $F(s)$ is finally formulated as

$$\frac{F(s)}{F_d(s)} = \frac{\left(s^2 + k_d s + k_p\right)\left(s^3 + l_1 s^2 + l_2 s + l_3\right)}{\frac{\alpha}{b}\left(s^2 + a_1 s + a_2\right)\left(s^3 + l_2 s^2 + l_1 s\right) + C(s)} \tag{23}$$

with

$$C(s) = \left(k_d s + k_p\right)\left(s^3 + l_1 s^2 + l_2 s\right) + l_3\left(s^2 + k_d s + k_p\right). \tag{24}$$

From the above transfer function, increasing $\frac{\alpha}{b}$ will decrease the bandwidth of the close-loop control system. With the help of simulation software MATLAB/Simulink, corresponding close-loop Bode diagram with the LESO-MFFC is drawn as Fig. 3.

As shown in Fig. 3, with the increase of α, the bandwidth of the controlled SEA is decreased. In the simulation, the actual control input gain b is set to be 1.45×10^6, which is calculated by product data-sheet [6]. When $\frac{\alpha}{b} \gg 1$, the bandwidth cannot satisfy the application requirements. When $\frac{\alpha}{b}$ is near 1 or $\frac{\alpha}{b} \ll 1$, the bandwidth is satisfactory. However, the bandwidth cannot be obviously increased by decreasing the $\frac{\alpha}{b}$ as $C(s)$ will play the dominant role in the denominator of (23). In this case, the transfer function can be considered as

$$\frac{F(s)}{F_d(s)} = \frac{\left(s^2 + k_d s + k_p\right)\left(s^3 + l_1 s^2 + l_2 s + l_3\right)}{\left(k_d s + k_p\right)\left(s^3 + l_1 s^2 + l_2 s\right) + l_3\left(s^2 + k_d s + k_p\right)} \tag{25}$$

The numerator's order is higher than the denominator's. This means that the control action may become too "fast" and causes possible chatter or even instability. The above analysis explains why the LESO-based control relies on a proper selection or estimate of the control input gain.

3.4. Enhanced extended state observer-based controller

In order to avoid the requirement for accurate selection of the control input gain α, a projected gradient estimator (PGE) [30] is integrated into the iPD control scheme. First, it is assumed that the unknown lumped disturbance d_{lumped} is limited by $\bar{d}$, that is $\left|d_{lumped}\right| \leq \bar{d}$. The only known information about α is the sign (positive in this study) and for avoiding singularity ($\alpha = 0$), α is limited by a lower bound α_{low}. Here the state space Eq. (15) is redefined as

$$\begin{cases} \dot{x}_1 = x_2 \\ \dot{x}_2 = x_3 \\ \dot{x}_3 = \dot{d}_{lumped} + \alpha \dot{u} \end{cases} \tag{26}$$

with a redefinition of x_3 as

$$x_3 = d_{lumped} + \alpha u. \tag{27}$$

Such a new definition of state enables us to view d_{lumped} and α as parameters to be estimated. According to the definition of *ultra-local model* in Eq. (9), x_3 is the force acceleration of the SEA. With the definition of the following vectors

$$\theta = \begin{bmatrix} d_{lumped} \\ \alpha \end{bmatrix}, \hat{\theta} = \begin{bmatrix} \hat{d}_{lumped} \\ \hat{\alpha} \end{bmatrix}, \varphi = \begin{bmatrix} 1 \\ u \end{bmatrix}, \tag{28}$$

we define a quadratic cost function as follow

$$J\left(\hat{\theta}\right) = \frac{1}{2}\left(x_3 - \hat{\theta}^T \varphi\right)^2. \tag{29}$$

According to the gradient method [30], the cost function $J\left(\hat{\theta}\right)$ can be minimized by following differential equation

$$\dot{\hat{\theta}} = -\gamma \nabla J\left(\hat{\theta}\right) = \gamma\left(x_3 - \hat{\theta}^T \varphi\right)\varphi, \tag{30}$$

where γ is a tunable convergence coefficient. The LESO is used to estimate the states in (26). By replacing the state x_3 by its estimation value $\hat{x}_3$ from the LESO, a novel enhanced ESO (EESO) is designed as

$$\begin{cases} \dot{\hat{x}}_1 = l_1\left(x_1 - \hat{x}_1\right) + \hat{x}_2 \\ \dot{\hat{x}}_2 = l_2\left(x_1 - \hat{x}_1\right) + \hat{x}_3 \\ \dot{\hat{x}}_3 = l_3\left(x_1 - \hat{x}_1\right) \\ \dot{\hat{d}}_{lumped} = \gamma w \\ \dot{\hat{\alpha}} = \begin{cases} 0, \text{if } \left(\hat{\alpha} = \alpha_{low}, wu < 0\right) \\ \gamma w u, \text{otherwise} \end{cases} \end{cases} \tag{31}$$

with the prediction error w defined as

$$w = \hat{x}_3 - \hat{\theta}^T \varphi. \tag{32}$$

With the proposed EESO, the novel MFFC is finally formulated as

$$u = \frac{1}{\hat{\alpha}}\left[\ddot{F}_d + k_d\left(\dot{F}_d - \hat{x}_2\right) + k_p e - \hat{d}_{lumped}\right] \tag{33}$$

For stability analysis, the observer error vector is redefined as

$$\varepsilon = \begin{bmatrix} x_1 - \hat{x}_1 \\ x_2 - \hat{x}_2 \\ x_3 - \hat{x}_3 \end{bmatrix} \triangleq \begin{bmatrix} \varepsilon_1 \\ \varepsilon_2 \\ \varepsilon_3 \end{bmatrix} \tag{34}$$

and the following state error dynamics can be deduced

$$\dot{\varepsilon} = A_\varepsilon \varepsilon + B_\varepsilon\left(\dot{d}_{lumped} + \alpha \dot{u}\right), A_\varepsilon = \begin{bmatrix} -l_1 & 1 & 0 \\ -l_2 & 0 & 1 \\ -l_3 & 0 & 0 \end{bmatrix}, B_\varepsilon = \begin{bmatrix} 0 \\ 0 \\ 1 \end{bmatrix}, \tag{35}$$

where A_ε is a Hurwitz matrix. Accordingly, the characteristic equation can be formulated as

$$\lambda_o(s) = s^3 + l_1 s^2 + l_2 s + l_3 = (s + \omega_o)^3 \tag{36}$$

By assigning all the eigenvalues at $-\omega_o$, the observer gains l_1, l_2, l_3 can be determined by a single parameter ω_o as

$$l_1 = 3\omega_o, l_2 = 3\omega_o^2, l_3 = \omega_o^3 \tag{37}$$

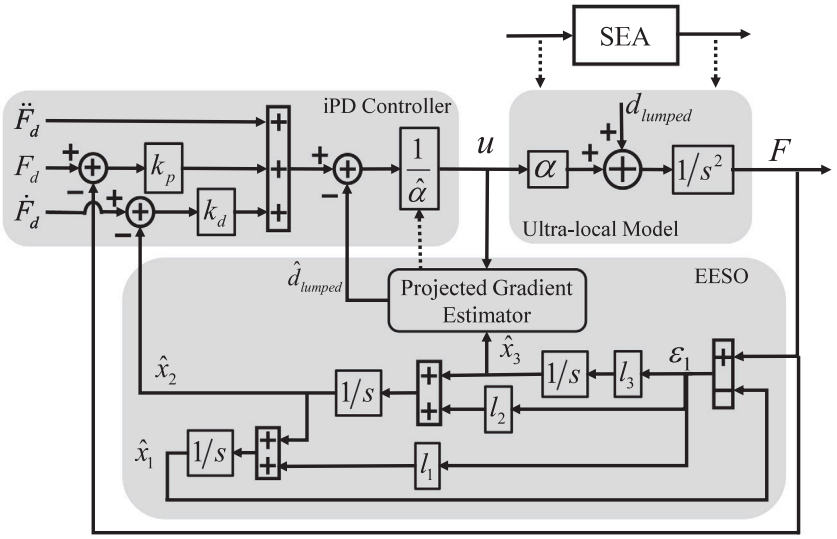

Fig. 4. Enhanced extended state observer (EESO)-based model-free force control (EESO-MFFC) scheme.

Here ω_o is called the observer bandwidth [19], which determines the performance of observer. Such a tuning method is also applicable to the determination of the parameters in Eq. (17).

By substituting the control law (33) to the *ultra-local model* (9), one can obtain

$$\begin{aligned}\ddot{F}&=\frac{\alpha}{\hat{\alpha}}\left[\ddot{F}_d+k_p e+k_d\left(\dot{F}_d-\hat{x}_2\right)-\hat{d}_{lumped}\right]+d_{lumped}\\&=\ddot{F}_d+k_p e+k_d\left(\dot{F}_d-x_2+x_2-\hat{x}_2\right)+\tilde{d}_{lumped}+\tilde{\alpha}u\\&=\ddot{F}_d+k_p e+k_d\dot{e}+k_d\varepsilon_2+\tilde{d}_{lumped}+\tilde{\alpha}u,\end{aligned}\tag{38}$$

where $\tilde{d}_{lumped}=d_{lumped}-\hat{d}_{lumped}, \tilde{\alpha}=\alpha-\hat{\alpha}$. The equation above can be reformulated as

$$\ddot{e}=-k_p e-k_d\dot{e}-k_d\varepsilon_2-\tilde{d}_{lumped}-\tilde{\alpha}u.\tag{39}$$

By defining the following error vectors

$$\tilde{\theta}=\theta-\hat{\theta}=\begin{bmatrix}\tilde{d}_{lumped}\\ \tilde{\alpha}\end{bmatrix}, E=\begin{bmatrix}e\\ \dot{e}\end{bmatrix},\tag{40}$$

the force error dynamics can be finally rewritten as

$$\dot{E}=A_E E+B_E\tilde{\theta}^T\varphi+C_E\varepsilon_2\tag{41}$$

with

$$A_E=\begin{bmatrix}0 & 1\\ -k_p & -k_d\end{bmatrix}, B_E=\begin{bmatrix}0\\ -1\end{bmatrix}, C_E=\begin{bmatrix}0\\ -k_d\end{bmatrix},\tag{42}$$

where A_E is a Hurwitz matrix and k_p, k_d can still be tuned according to (14).

The entire control scheme can be described as Fig. 4.

As shown in Fig. 4, the force dynamics of the SEA is firstly considered as an equivalent second-order *ultra-local model* with an undetermined control input gain α and an unknown *lumped total disturbance* d_{lumped}. Then an EESO is proposed to estimate d_{lumped}, α and $\dot{F}$ simultaneously. With the estimation results of the EESO, an intelligent PD (iPD) control scheme is realized, which is robust to disturbance and easy to be tuned by zero-pole placement.

To show the close-loop frequency response with different initial values of the control input gain, the simulation similar to Fig. 3 was conducted and the Bode diagram is given as Fig. 5. By comparing Fig. 5 to Fig. 3, we can conclude that the proposed EESO-MFFC method can effectively enlarge the close-loop bandwidth of the LESO-MFFC and reduce the phase lag when improperly large α_0 is selected.

Theorem 1. *Consider the SEA dynamics denoted by the equivalent state space Eq. (26) and suppose* $\dot{x}_3=\dot{d}_{lumped}+\alpha\dot{u}$ *is bounded. With the proposed force controller (33) based on the EESO (31), there exists a finite time* t_c *s.t.,*

$$\|E\|=\mathrm{O}\left(\frac{1}{\sqrt{\omega_o}}\right)+\mathrm{O}\left(\frac{1}{\sqrt{\gamma}}\right), t>t_c,\tag{43}$$

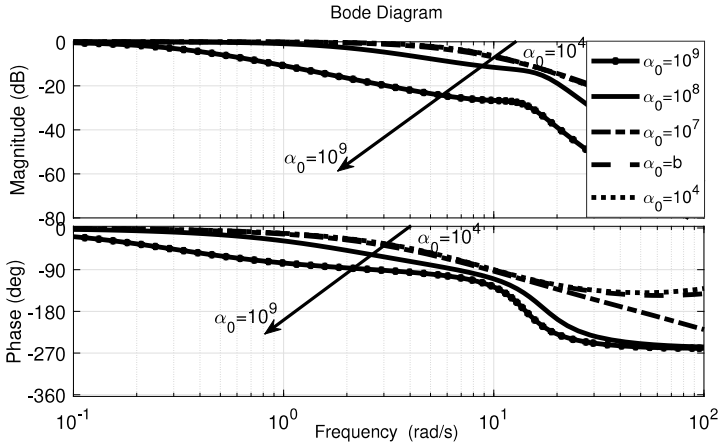

Fig. 5. Close-loop Bode diagram under the proposed EESO-MFFC method with different initial control input gain α_0.

where the operator $\mathrm{O}(\bullet)$ *means the value of the same magnitude as its argument.*

Proof. A Lyapunov function is designed as

$$V = E^T P_1 E + \varepsilon^T P_2 \varepsilon + \frac{1}{2k}\tilde{\theta}^T\tilde{\theta}, \tag{44}$$

where $k > 0$ and P_1, P_2 are positive definite matrixes satisfying

$$P_1 A_E + A_E^T P_1 = -I, P_2 A_\varepsilon + A_\varepsilon^T P_2 = -I. \tag{45}$$

For the convenience of proof, the Lyapunov function is considered to be composed of following three terms

$$V_1 = E^T P_1 E, V_2 = \varepsilon^T P_2 \varepsilon, V_3 = \frac{1}{2k}\tilde{\theta}^T\tilde{\theta}. \tag{46}$$

By taking the derivative of V_1 and combining the tracking error dynamic(41), we have

$$\begin{aligned}\dot{V}_1 &= \dot{E}^T P_1 E + E^T P_1 \dot{E}\\ &= \left[A_E E + B_E\tilde{\theta}^T\varphi + C_E\varepsilon_2\right]^T P_1 E + E^T P_1 \times \left[A_E E + B_E\tilde{\theta}^T\varphi + C_E\varepsilon_2\right]\\ &= E^T\left(A_E^T P_1 + P_1 A_E\right)E + 2\tilde{\theta}^T\varphi B_E^T P_1 E + 2\varepsilon_2 C_E^T P_1 E\\ &= -\|E\|^2 + 2\tilde{\theta}^T\varphi B_E^T P_1 E + 2\varepsilon_2 C_E^T P_1 E.\end{aligned} \tag{47}$$

By taking the derivative of V_2 and combining the observer error dynamic (35), we have

$$\begin{aligned}\dot{V}_2 &= \dot{\varepsilon}^T P_2\varepsilon + \varepsilon^T P_2\dot{\varepsilon}\\ &= \left[A_\varepsilon\varepsilon + B_\varepsilon\left(\dot{d}_{lumped} + \alpha\dot{u}\right)\right]^T P_2\varepsilon + \varepsilon^T P_2 \times \left[A_\varepsilon\varepsilon + B_\varepsilon\left(\dot{d}_{lumped} + \alpha\dot{u}\right)\right]\\ &= \varepsilon^T\left(A_\varepsilon^T P_2 + P_2 A_\varepsilon\right)\varepsilon + \left(\dot{d}_{lumped} + \alpha\dot{u}\right)B_\varepsilon^T P_2\varepsilon + \varepsilon^T P_2 B_\varepsilon\left(\dot{d}_{lumped} + \alpha\dot{u}\right)\\ &= -\|\varepsilon\|^2 + 2\left(\dot{d}_{lumped} + \alpha\dot{u}\right)B_\varepsilon^T P_2\varepsilon.\end{aligned} \tag{48}$$

By taking the derivative of V_3, we have

$$\dot{V}_3 = \tfrac{1}{k}\tilde{\theta}^T\left(\dot{\theta} - \dot{\hat{\theta}}\right) \le \tfrac{1}{k}\tilde{\theta}^T\left(\dot{\theta} - \gamma w\varphi\right). \tag{49}$$

As w can be rewritten as

$$w = \hat{x}_3 - x_3 + x_3 - \left(\hat{d}_{lumped} + \hat{\alpha}u\right) = \tilde{\theta}^T\varphi - \varepsilon_3, \tag{50}$$

$\dot{V}_3$ can be further deduced as

$$\dot{V}_3 \le \frac{1}{k}\tilde{\theta}^T\dot{\theta} - \frac{1}{k}\gamma\tilde{\theta}^T\left(\tilde{\theta}^T\varphi - \varepsilon_3\right)\varphi = -\frac{1}{k}\gamma\left(\tilde{\theta}^T\varphi\right)^2 + \frac{1}{k}\gamma\tilde{\theta}^T\varphi\varepsilon_3 + \frac{1}{k}\tilde{\theta}^T\dot{\theta}. \tag{51}$$

By summing $\dot{V}_1$, $\dot{V}_2$ and $\dot{V}_3$, one obtains

$$\begin{aligned}\dot{V} &= \dot{V}_1 + \dot{V}_2 + \dot{V}_3\\ &\le -\|E\|^2 - \|\varepsilon\|^2 - \frac{1}{k}\gamma\left(\tilde{\theta}^T\varphi\right)^2 + \tilde{\theta}^T\varphi\left(\frac{\gamma}{k}\varepsilon_3 + 2B_E^T P_1 E\right)\\ &+ \frac{1}{k}\tilde{\theta}^T\dot{\theta} + 2\varepsilon_2 C_E^T P_1 E + 2\left(\dot{d}_{lumped} + \alpha\dot{u}\right)B_\varepsilon^T P_2\varepsilon.\end{aligned} \tag{52}$$

As the following inequality holds,

$$\begin{aligned}&\left(\tilde{\theta}^T\varphi\right)\sqrt{\frac{2\gamma}{k}}\sqrt{\frac{k}{2\gamma}}\left(\frac{\gamma}{k}\varepsilon_3+2B_E^TP_1E\right)\\&\le\frac{1}{2}\left[\left(\tilde{\theta}^T\varphi\right)\sqrt{\frac{2\gamma}{k}}\right]^2+\left(\sqrt{\frac{k}{2\gamma}}\frac{\gamma}{k}\varepsilon_3\right)^2+\left(2\sqrt{\frac{k}{2\gamma}}B_E^TP_1E\right)^2\\&=\frac{\gamma}{k}\left(\tilde{\theta}^T\varphi\right)^2+\frac{\gamma}{2k}\varepsilon_3^2+\frac{2k}{\gamma}\left(B_E^TP_1E\right)^2,\end{aligned}\tag{53}$$

we have

$$\begin{aligned}\dot{V}&=-\|E\|^2-\|\varepsilon\|^2+\frac{\gamma}{2k}\varepsilon_3^2+\frac{2k}{\gamma}\left(B_E^TP_1E\right)^2+2\varepsilon_2C_E^TP_1E\\&+\frac{1}{k}\tilde{\theta}^T\dot{\theta}+2\left(\dot{d}_{lumped}+\alpha\dot{u}\right)B_\varepsilon^TP_2\varepsilon\\&\le-\|E\|^2-\|\varepsilon\|^2+\frac{\gamma}{2k}\varepsilon_3^2+\frac{2k}{\gamma}\left(B_E^TP_1E\right)^2+\frac{\gamma}{2k}\varepsilon_2^2+\frac{2k}{\gamma}\\&\times\left(C_E^TP_1E\right)^2+\frac{1}{k}\tilde{\theta}^T\dot{\theta}+2\left(\dot{d}_{lumped}+\alpha\dot{u}\right)B_\varepsilon^TP_2\varepsilon\\&=-\|E\|^2-\|\varepsilon\|^2+\frac{\gamma}{2k}\left(\varepsilon_2^2+\varepsilon_3^2\right)+\frac{2k}{\gamma}\left[\left(B_E^T+C_E^T\right)P_1E\right]^2\\&+\frac{1}{k}\tilde{\theta}^T\dot{\theta}+2\left(\dot{d}_{lumped}+\alpha\dot{u}\right)B_\varepsilon^TP_2\varepsilon\\&\le-\|E\|^2-\|\varepsilon\|^2+\frac{\gamma}{2k}\|\varepsilon\|^2+\frac{2k}{\gamma}\left(1+k_d\right)^2\|P_1\|^2\|E\|^2\\&+\frac{1}{k}\tilde{\theta}^T\dot{\theta}+2\left(\dot{d}_{lumped}+\alpha\dot{u}\right)B_\varepsilon^TP_2\varepsilon.\end{aligned}\tag{54}$$

Now by defining

$$m=\max\left\{\frac{\gamma}{2k},\frac{2k}{\gamma}\left(1+k_d\right)^2\|P_1\|^2\right\}\tag{55}$$

we can make $m<1$ by choosing appropriate parameters as $\|P_1\|^2$ is determined by ω_o. By choosing $k=\frac{\gamma}{4(1+k_d)\|P_1\|^2}$, we have $\frac{2k}{\gamma}\left(1+k_d\right)^2\|P_1\|^2=\frac{1}{2}$. In addition, by increasing the bandwidth of ESO, it is easy to obtain

$$\frac{\gamma}{2k}=2\left(1+k_d\right)^2\|P_1\|^2<1.\tag{56}$$

Therefore, it can further be concluded that

$$\begin{aligned}\dot{V}&\le-\|E\|^2-\|\varepsilon\|^2+m\|\varepsilon\|^2+m\|E\|^2+\frac{1}{k}\tilde{\theta}^T\dot{\theta}+2\left(\dot{d}_{lumped}+\alpha\dot{u}\right)B_\varepsilon^TP_2\varepsilon\\&=-\left(1-m\right)V+\frac{1-m}{2k}\tilde{\theta}^T\tilde{\theta}+\frac{1}{k}\tilde{\theta}^T\dot{\theta}+2\left(\dot{d}_{lumped}+\alpha\dot{u}\right)B_\varepsilon^TP_2\varepsilon.\end{aligned}\tag{57}$$

According to the results in [31], there exists a finite time t_o such that $\|\varepsilon\|=\mathrm{O}\left(\frac{1}{\omega_o}\right), t>t_o$. With the bounded assumption of $\left(\dot{d}_{lumped}+\alpha\dot{u}\right)$, one has

$$2\left(\dot{d}_{lumped}+\alpha\dot{u}\right)B_\varepsilon^TP_2\varepsilon=\mathrm{O}\left(\frac{1}{\omega_o}\right).\tag{58}$$

Besides, k,γ are set to have the same magnitude such that

$$\frac{1-m}{2k}\tilde{\theta}^T\tilde{\theta}+\frac{1}{k}\tilde{\theta}^T\dot{\theta}=\mathrm{O}\left(\frac{1}{\gamma}\right).\tag{59}$$

In conclusion, with the Comparison Principle, the final solution for Lyapunov function V is obtained as

$$V\le V\left(t_0\right)e^{-(1-m)(t-t_0)}+\mathrm{O}\left(\frac{1}{\omega_o}\right)+\mathrm{O}\left(\frac{1}{\gamma}\right).\tag{60}$$

Therefore, there exists a finite time t_c that make (43) hold.

According to Theorem 1, robust and accurate force control of the SEA can be performed with proper tuning of ω_o,ω_c and γ. The PGE does not have to make a good estimation of the control input gain α as the proposed controller only aims to achieve the minimal force tracking error. Accurate force tracking is achieved by a composite effect from the adaptive $\hat{\alpha}$ and $\hat{d}_{lumped}$.

4. Experimental results

In this section, the proposed EESO-based MFFC (EESO-MFFC) is verified with implementations to a single-joint SEA-driven robotic arm in different conditions. The SEA-driven robotic arm is shown in Fig. 6.

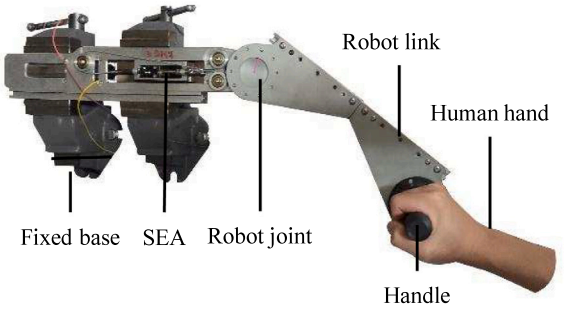

Fig. 6. A SEA-driven robotic arm.

Table 2
RMSE of the force tracking.

Controller	$\alpha_0 = 10^4$	$\alpha_0 = 10^6$	$\alpha_0 = 10^7$	$\alpha_0 = 10^8$
LESO-MFFC	7.6409	8.3403	43.4029	50.3329
EESO-MFFC	5.1765	5.9125	3.0459	3.4201

The real-time control platform is equipped with the dSPACE 1007 control board (DS1007), which runs a Real-Time Operation System (RTOS). The platform is also embedded with other I/O boards including the DS3002 counter board for collecting the encoder signals, the DS2102 DAC board for generating control signals and the DS2002 ADC board for collecting potentiometer signals. A DS1007 modular system is assembled from the DS1007 PPC Processor Board, which uses a Freescale P5020 processor as the real-time processor. The processor controls all the connected I/O boards via the PHS bus. The control program is specified in MATLAB/Simulink software and then loaded from the host PC to the DS1007 control board for real-time control. The dSPACE platform communicates the control command to the Elmo driver (Gold DC Whistle) by sending analog voltage signal with DS2102 DAC board. The Elmo driver is utilized to drive the brushless motor (Maxon EC-4pole) and it acts as a low-level processor and generates the PWM action signals, whose switching frequency is 22 kHz in the advanced unipolar way. To verify the proposed EESO-MFFC method, comparative experiments will be conducted.

4.1. Comparing with the LESO-MFFC method

As described in Section III Part B, the selection of the control input gain α will have great impact on the control performance of the LESO-MFFC. In this case, we implement the LESO-MFFC with different selections of the control input gain α and show the effects of these selections. Then, for comparison, we select the same values as the initial values of the control input gain (denoted as α_0) in the proposed EESO-MFFC.

After some tuning effort, the control parameters in (14) and (37) are set as $\omega_c = 10$ rad/s, $\omega_o = 200$ rad/s. It is well-known that higher bandwidth means better command following, robustness and sensitivity to parameter variations. Meanwhile, achievable bandwidth is limited by the presence of sensor noise and dynamic uncertainties (friction, backlash, etc.). During applications, we gradually increase the controller bandwidth ω_c until physical constraints are met, which means control signal becomes excessively noisy or instability arises (oscillatory behavior). Then a suitable parameter $\omega_c = 10$ is determined without much difficulty. In [19], the observer bandwidth ω_o is recommended to be several times larger than the controller bandwidth ω_c. This is physically reasonable as in a closed-loop feedback control system the observer should possess higher bandwidth so that it can provide effective state or disturbance estimation to the control input. During applications, we initially set $\omega_o = \omega_c$ and then gradually increase ω_o until physical constraints are met, which means control signal becomes excessively noisy or instability arises (oscillatory behavior). Then a suitable parameter $\omega_o = 200$ rad/s is determined without much difficulty.

According to the results of theoretical calculation or identification result (61), the magnitude of α is close to 10^6. From Fig. 7, the LESO-MFFC can achieve satisfactory control performance with $\alpha = 10^6$. However, if the magnitude of α is decreased, the force tracking becomes shaky as the controller becomes sensitive to error and noise. When the magnitude of α is increased, effective force tracking is not available because of low control bandwidth. These experimental results are consistent with the analysis in Section 3, Part C.

In contrast, the EESO-MFFC can always guarantee accurate tracking with different magnitude of α_0. For more quantitative demonstration, the root-mean-square-errors (RMSE) of the force tracking results in Fig. 7 are calculated and summarized in Table 2.

According to the estimation results of $\hat{\alpha}$ with different initial values α_0 in Fig. 8, $\hat{\alpha}$ does not need to converge to a specific α. The EESO-MFFC can always guarantee accurate and stable force tracking.

In the application of the LESO-MFFC method, α can be selected according to the theoretical analysis or the identification results and then tune it around such values. This provides a basic principle for determining the control input gain. However, when the

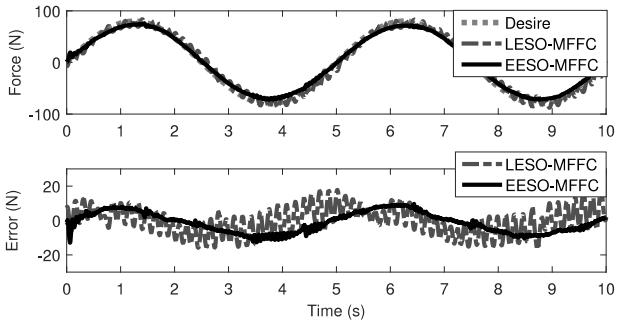

(a) $\alpha = \alpha_0 = 10^4$

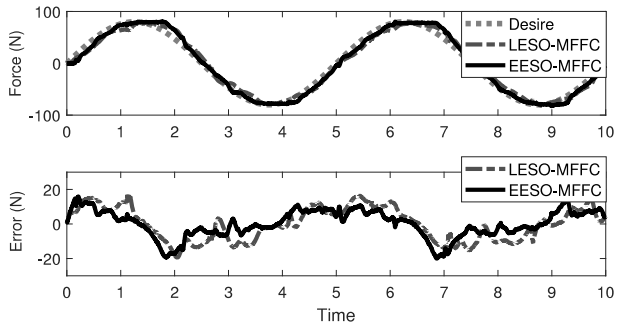

(b) $\alpha = \alpha_0 = 10^6$

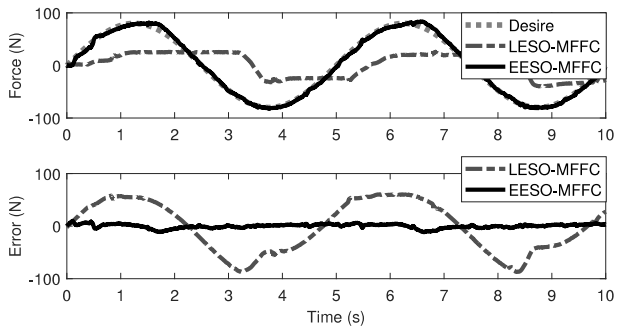

(c) $\alpha = \alpha_0 = 10^7$

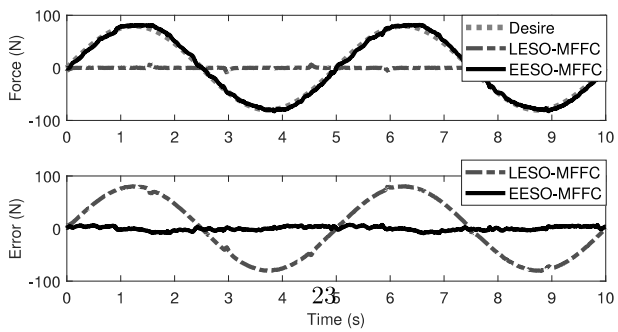

(d) $\alpha = \alpha_0 = 10^8$

Fig. 7. Control performance of the LESO-MFFC and the EESO-MFFC with different control input gain α $(10^4, 10^6, 10^7, 10^8)$ and different initial values α_0 $(10^4, 10^6, 10^7, 10^8)$.

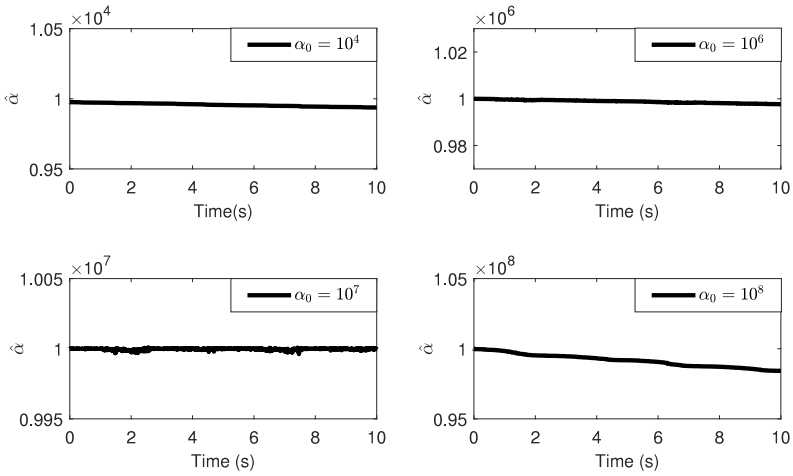

Fig. 8. Estimation values of α with different initial value α_0.

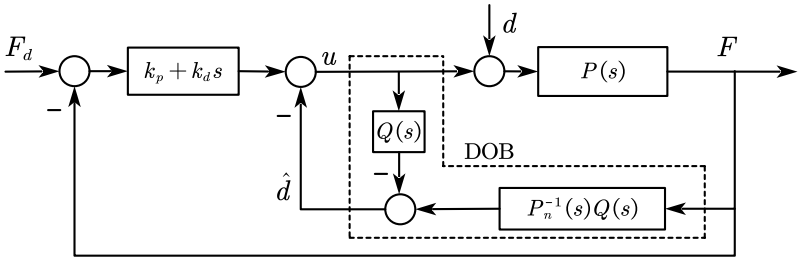

Fig. 9. Conventional disturbance observer-based control structure. $Q(s)$ denotes the low-pass filter for the realization of DOB and it was chosen as a 2nd-order filter.

control input gain α is difficult to identify (nonlinear or time-varying) or there is a large mismatch between the selected α and the optimal one, the performance of the control performance will deteriorate. That is the reason that the LESO-MFFC method fails to achieve satisfactory force control in Fig. 7(a), (c) and (d). However, such a requirement in the proposed EESO-MFFC is removed. The initial value of the control input gain can be selected in a large range and this provides good robustness during the parametric tuning process. Besides, strict convergence to the real value of α is not necessary as the control target is just force tracking and the tuning of control parameters is following the principle of minimizing force error.

4.2. Comparing with other popular controllers

To further demonstrate the effectiveness of the EESO-MFFC, comparative experiments are conducted with three controllers: a classical PID controller with friction compensation (PID-FC), a widely adopted disturbance observer-based controller (DOBC) [3,9] and the proposed EESO-MFFC. With the MATLAB identification toolbox, the force dynamics of the SEA is identified as

$$P_n(s) = \frac{5.915 \times 10^5}{s^2 + 7.738s + 188.36} \tag{61}$$

In addition, the authors use a typical static friction model in [32] to identify the friction model. It is formulated with the control current as

$$u(v) = 2\left\{0.22 + 0.08e^{\left(-\left|\frac{v}{2}\right|\right)} + 0.0005\,|v|\right\} sat\left(\frac{v}{2}\right) \tag{62}$$

where v denotes force velocity. The PID-FC controller is designed as

$$u = k_p e + k_i \int e + k_d \dot{e} + u(v)\,. \tag{63}$$

where k_p, k_i, k_d are PID control gains. The DOBC structure can be described as Fig. 9. Both of the controllers above are designed according to the identified force model (61).

Figs. 10 and 11 show the comparative results of control at a low force frequency (0.3 Hz) and a high force frequency (3 Hz) respectively. As the PID-FC controller cannot perform stable high-frequency force tracking due to its phase lag, only the results of

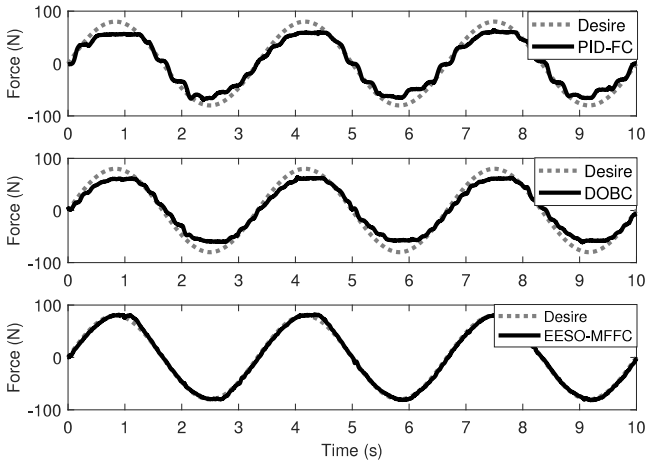

(a) Tracking results

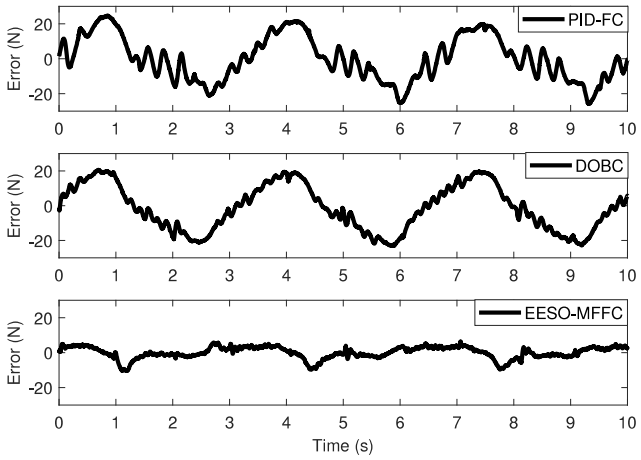

(b) Tracking errors

Fig. 10. 0.3 Hz force tracking under different controllers.

DOBC and EESO-MFFC are shown in Fig. 11. With PID-FC controller, the friction force and uncertainties may still cause resonance when PID parameters are higher. This limits the improvement of control performance and may even cause damage to the SEA-driven robotic arm or to the human. The DOBC can perform effective tracking, but its performance is still limited by modeling mismatch and noisy differential signals. With the proposed EESO-MFFC, the performance of force tracking get fundamentally improved.

As a direct feedback and error-driven controller, PID control can be strengthened by friction compensation or other possible feedforward control. However, it will be limited by the single degree-of-freedom design. In our target applications, PID-type controller does not provide specific treatment to the external disturbance. Besides, the measurement noise and saturation will further limit the increase of PID gains, which makes it difficult to improve the control performance. The DOBC utilizes the identified dynamic model and low-pass filter to estimate the external disturbing effects and then compensates the disturbance by feeding the estimated value to the control input. Such an active disturbance rejective control scheme 9 can improve the robustness of the close-loop system. While in our study, the modeling mismatch and measurement noise from analog signals limit the improvement of control performance. As low-pass filter-based differentiator is adopted in the DOBC, the differential precision is sacrificed for filtering noise and guaranteeing stable control. For the proposed EESO-MFFC, the requirement for model identification is removed and a 2 degree-of-freedom controller is constructed with observer and feedback control. The EESO can simultaneously estimate the disturbance and force velocity (differential signal), whose performance will be determined by the bandwidth parameter ω_o. The feedback control bandwidth is determined by ω_c. The two parameters provide physically meaningful principle of control tuning. Higher values mean higher robustness and accuracy. The control objective can be more effectively achieved without violating the physical constrains.

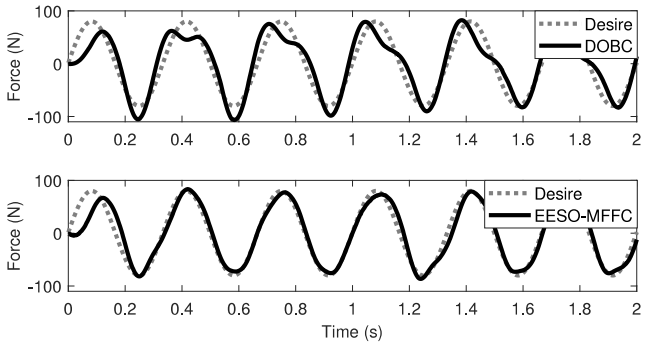

(a) Tracking results

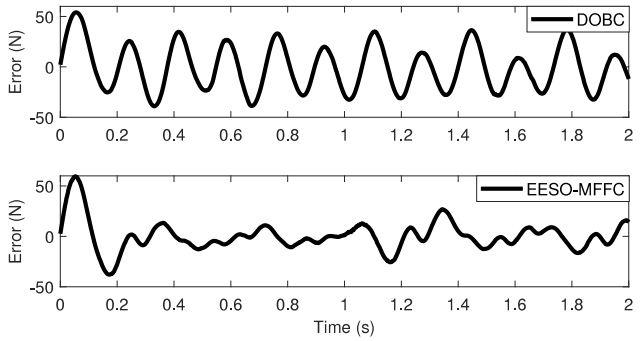

(b) Tracking errors

Fig. 11. 3 Hz force tracking under different controllers.

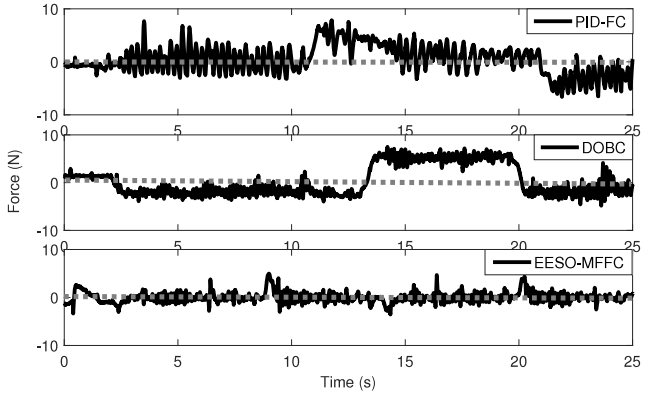

Fig. 12. Zero force control under different controllers.

4.3. Zero force control and joint-level impedance control

To further verify the potential of the EESO-MFFC in SEA-driven robots, zero force control and joint-level impedance control experiments are also conducted. During each test, the operator moves the robotic arm between two positions. The reflective force changes of the SEA can demonstrate the performance of zero force control.

With the proposed force controller as an inner-loop control, a joint-level impedance control is performed. The desired force command is generated as

$$F_d = -\frac{Kq}{r}, \tag{64}$$

where $K = 0.035$ Nm/° denotes the defined joint stiffness. During each tests, the operator will move the robotic arm away from the initial position and then release it. Such movements will be repeated several times under different controllers.

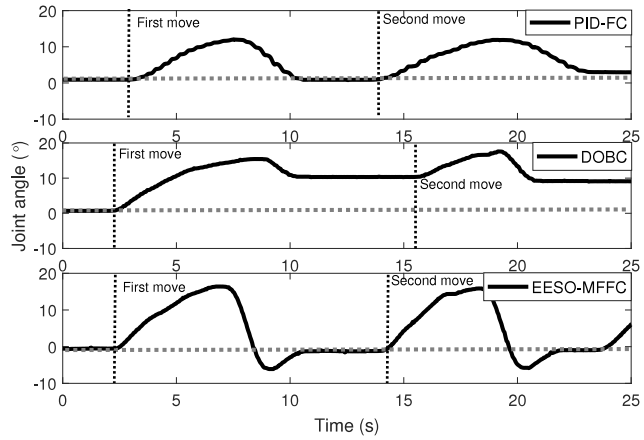

(a) Joint recovery

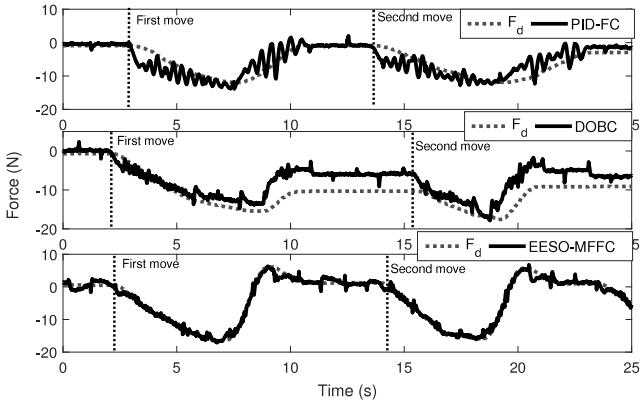

(b) Force tracking

Fig. 13. Impedance control under different controllers.

From Fig. 12 the PID-FC controller causes obvious chattering during zero force control. This may result in instability or resonance during implementations. The DOBC can hardly achieve high accuracy. With the proposed EESO-MFFC, the best backdrivability is achieved with minimal reflective force. The operator's moving process is free and smooth. Fig. 13 shows the performance of the joint-level impedance control with different controllers while the operator moves the SEA-driven robotic arm twice.

Fig. 13(a) shows the joint recovery performance and Fig. 13(b) shows the performance of tracking the desired force generated from Eq. (64). The PID-FC controller causes some fluctuations and the DOBC cannot perform effective recovery to the equilibrium point due to inaccurate force tracking. The proposed EESO-MFFC can achieve satisfactory and stable recovery to the equilibrium point with accurate force tracking. For quantitatively demonstrating the advantageous performance of the proposed method, the RMSE of the results in Fig. 13(b) are calculated and they are 3.4257 N (PID-FC), 3.9115 N (DOBC) and 0.9039 N (EESO-MFFC).

5. Conclusion

In this paper, a novel enhanced extended state observer (EESO)-based model-free force control (EESO-MFFC) method is proposed for a SEA-driven robot. It is constructed with the concept of *ultra-local model* and relies only on the input–output measurement. Comparative experiments demonstrate that the proposed EESO-MFFC can further relax the requirements for modeling information compared to existing model-free controller. With the disturbance rejection capability of the EESO, the force controller guarantees accurate force control and robustness to external disturbance. Through the tests of continuous force tracking, zero force control and impedance control, the advantageous performance of the EESO-MFFC is verified.

Meanwhile, the control flexibility is somehow sacrificed for making the controller easy to be tuned and extended to other linear SEAs. It also has good potential to be extended to nonlinear SEA or variable stiffness actuators (VSA), although some improvements on the adaptability may be necessary. Our future work will focus on the improvement of such a force controller (noise restraining, extension to other compliant actuators, etc.) and its implementation on rehabilitation tasks with an SEA-driven robot.

Declaration of competing interest

The authors declare that they have no known competing financial interests or personal relationships that could have appeared to influence the work reported in this paper.

References

[1] G.A. Pratt, M.M. Williamson, Series elastic actuators, in: Proceedings 1995 IEEE/RSJ International Conference on Intelligent Robots and Systems, Vol. 1, 1995, pp. 399–406.
[2] H. Yu, S. Huang, G. Chen, Y. Pan, Z. Guo, Human-robot interaction control of rehabilitation robots with series elastic actuators, IEEE Trans. Robot. 31 (5) (2015) 1089–1100.
[3] N. Paine, J.S. Mehling, J. Holley, N.A. Radford, G. Johnson, C.-L. Fok, L. Sentis, Actuator control for the NASA-JSC valkyrie humanoid robot: A decoupled dynamics approach for torque control of series elastic robots, J. Field Robotics 32 (3) (2015) 378–396.
[4] E. Basafa, M. Sheikholeslami, A. Mirbagheri, F. Farahmand, G.R. Vossoughi, Design and implementation of series elastic actuators for a haptic laparoscopic device, in: IEEE Engineering in Medicine and Biology Society. Conference, Vol. 2009, 2009, pp. 6054–6057.
[5] D. Robinson, Design and Analysis of Series Elasticity in Closed-Loop Actuator Force Control (Ph.D. thesis), Massachusetts Institute Of Technology, 2000.
[6] H. Yu, S. Huang, G. Chen, N. Thakor, Control design of a novel compliant actuator for rehabilitation robots, Mechatronics 23 (8) (2013) 1072–1083.
[7] K. Kong, J. Bae, M. Tomizuka, A compact rotary series elastic actuator for human assistive systems, IEEE/ASME Trans. Mechatronics 17 (2) (2012) 288–297.
[8] Y. Lin, Z. Chen, B. Yao, Decoupled torque control of series elastic actuator with adaptive robust compensation of time-varying load-side dynamics, IEEE Trans. Ind. Electron. 67 (7) (2019) 5604–5614.
[9] K. Kong, J. Bae, M. Tomizuka, Control of rotary series elastic actuator for ideal force-mode actuation in human-robot interaction applications, IEEE/ASME Trans. Mechatronics 14 (1) (2009) 105–118.
[10] E. Sariyildiz, R. Mutlu, H. Yu, A sliding mode force and position controller synthesis for series elastic actuators, Robotica 38 (1) (2020) 15–28.
[11] E. Sariyildiz, S. Hiromu, N. Takahiro, U. Barkan, O. Kouhei, A stability analysis for the acceleration-based robust position control of robot manipulators via disturbance observer, IEEE/ASME Trans. Mechatronics 23 (5) (2018) 2369–2378.
[12] Y. Pan, X. Li, H. Wang, H. Yu, Continuous sliding mode control of compliant robot arms: A singularly perturbed approach, Mechatronics 52 (2018) 127–134.
[13] X. Li, Y. Liu, H. Yu, Iterative learning impedance control for rehabilitation robots driven by series elastic actuators, Automatica 90 (2018) 1–7.
[14] W. Wang, J. Ma, X. Li, Z. Cheng, H. Zhu, C.S. Teo, T.H. Lee, Iterative super-twisting sliding mode control for tray indexing system with unknown dynamics, IEEE Trans. Ind. Electron. (2020).
[15] M. Fliess, C. Join, Model-free control, Int. J. Control Taylor 86 (12) (2013) 2228–2252.
[16] H.P. Wang, X.F. Ye, Y. Tian, G. Zheng, N. Christov, Model-free-based terminal SMC of quadrotor attitude and position, IEEE Trans. Aerosp. Electron. Syst. 52 (5) (2016) 2519–2528.
[17] J.Q. Han, From PID to active disturbance rejection control, IEEE Trans. Ind. Electron. 56 (3) (2009) 900–906.
[18] M. Hosseini-Pishrobat, J. Keighobadi, Robust output regulation of a triaxial MEMS gyroscope via nonlinear active disturbance rejection, Internat. J. Robust Nonlinear Control 28 (5) (2018) 1830–1851.
[19] Z. Gao, Scaling and bandwidth-parameterization based controller tuning, in: Proceedings of the American Control Conference, Vol. 6, American, 2003, pp. 4989–4996.
[20] W. Xue, W. Bai, S. Yang, K. Song, Y. Huang, H. Xie, ADRC with adaptive extended state observer and its application to air–fuel ratio control in gasoline engines, IEEE Trans. Ind. Electron. 62 (9) (2015) 5847–5857.
[21] Z. Pu, R. Yuan, J. Yi, X. Tan, A class of adaptive extended state observers for nonlinear disturbed systems, IEEE Trans. Ind. Electron. 62 (9) (2015) 5858–5869.
[22] S. Lu, C. Tian, P. Yan, Adaptive extended state observer-based synergetic control for a long-stroke compliant microstage with stress stiffening, IEEE/ASME Trans. Mechatronics 25 (1) (2020) 259–270.
[23] W. Deng, J. Yao, Extended-state-observer-based adaptive control of electrohydraulic servomechanisms without velocity measurement, IEEE/ASME Trans. Mechatronics 25 (3) (2019) 1151–1161.
[24] L. Zhao, H. Cheng, Y. Xia, B. Liu, Angle tracking adaptive backstepping control for a mechanism of pneumatic muscle actuators via an AESO, IEEE Trans. Ind. Electron. 66 (6) (2019) 4566–4576.
[25] R. Chi, Y. Hui, B. Huang, Z. Hou, Active disturbance rejection control for nonaffined globally Lipschitz nonlinear discrete-time systems, IEEE Trans. Automat. Control (2021).
[26] T. Jiang, C. Huang, L. Guo, Control of uncertain nonlinear systems based on observers and estimators, Automatica 59 (2015) 35–47.
[27] L.B. Freidovich, H.K. Khalil, Performance recovery of feedback-linearization-based designs, IEEE Trans. Automat. Control 53 (10) (2008) 2324–2334.
[28] Y. Huang, W.X.C. Zhao, Active disturbance rejection control: methodology and theoretical analysis, ISA Trans. 53 (4) (2014) 963–976.
[29] W. Xue, Y. Huang, On frequency-domain analysis of ADRC for uncertain system, in: 2013 American Control Conference, 2013, pp. 6637–6642.
[30] P.A. Ioannou, J. Sun, Robust Adaptive Control, Courier Corporation, 2012.
[31] Q. Zheng, L.Q. Gao, Z. Gao, On stability analysis of active disturbance rejection control for nonlinear time-varying plants with unknown dynamics, in: 2007 46th IEEE Conference on Decision and Control, 2007, pp. 3501–3506.
[32] J. Zamberi, V.B. Hendrik, S. Jan, Friction compensation of an XY feed table using friction-model-based feedforward and an inverse-model-based disturbance observer, IEEE Trans. Ind. Electron. 56 (10) (2009) 3848–3853.